

Hyperfine field and electronic structure of magnetite below the Verwey transition

R. Řezníček,* V. Chlan, and H. Štěpánková

Faculty of Mathematics and Physics, Charles University in Prague, V Holešovičkách 2, 180 00 Prague 8, Czech Republic

P. Novák

Institute of Physics, ASCR, Cukrovarnická 10, 162 00 Prague 6, Czech Republic

(Received 17 September 2014; revised manuscript received 12 January 2015; published 23 March 2015)

Magnetite represents a prototype compound with a mixed valence of iron cations. Its structure and electron ordering below the Verwey transition have been studied for decades. A recently published precise crystallographic structure [Senn *et al.*, *Nature (London)* **481**, 173 (2012)] accompanied by a suggestion of a “trimeron” model has given a new impulse to magnetite research. Here we investigate hyperfine field anisotropy in the Cc phase of magnetite by quantitative reanalysis of published measurements of the dependences of the ^{57}Fe nuclear magnetic resonance frequencies on the external magnetic field direction. Further, *ab initio* density-functional-theory-based calculations of hyperfine field depending on the magnetization direction using the recently reported crystal structure are carried out, and analogous hyperfine anisotropy data linked to particular crystallographic sites are determined. These two sets of data are compared, and mutually matching groups of the iron B sites in the 8:5:3 ratio are found. Moreover, information on electronic structure is obtained from the *ab initio* calculations. Our results are compared with the trimeron model and with an alternative analysis [Patterson, *Phys. Rev. B* **90**, 075134 (2014)] as well.

DOI: [10.1103/PhysRevB.91.125134](https://doi.org/10.1103/PhysRevB.91.125134)

PACS number(s): 31.30.Gs, 71.15.Mb, 76.60.–k

I. INTRODUCTION

Magnetite is a prototype compound with a mixed cation valence. Its formal valence composition is $(\text{Fe}^{3+})_A(\text{Fe}^{3+}\text{Fe}^{2+})_B\text{O}_4$, where A and B refer to tetrahedrally and octahedrally coordinated sites, respectively. It crystallizes in the inverse cubic spinel structure ($Fd\bar{3}m$), which undergoes a first-order phase transition to the monoclinic Cc structure at the Verwey temperature $T_V \sim 120$ K. The mechanism of the transition, the character of the low-temperature structure, the ordering of cations, and their orbitals below T_V have been studied for several decades (as reviewed, e.g., in Refs. [1–3]) and still present intensively investigated topics [4–9]. Recently, using high-energy x-ray diffraction, Senn *et al.* [10] found that to a first approximation the original Verwey hypothesis [11] is adequate, although there are important deviations. To explain them, Senn *et al.* introduced “trimerons,” which may be important quasiparticles not only in magnetite above T_V [12] but also in other transition metal oxides. Moreover, trimerons seem to play a crucial role in the mechanism of the Verwey transition [13].

In magnetite all iron ions are in a high-spin state. Fe(A) on the tetrahedral sublattice are trivalent with the half-filled $3d$ shell. In the B sublattice, the octahedral crystal field splits the d states into a higher e_g doublet and a lower t_{2g} triplet. The five $3d$ electrons fill the e_g and t_{2g} majority-spin states, and the remaining electrons (one electron per two B sites) enter the minority-spin t_{2g} levels.

Trimerons are linear objects consisting of three Fe(B) ions. Bonds between these ions are typically shorter than the average Fe(B)-Fe(B) distances. The central ion is Fe^{2+} -like, and it donates part of its minority-spin t_{2g} electron to the remaining two Fe^{3+} -like ions. The charge distribution is described and

qualitatively analyzed in Ref. [10]. Trimerons are linked together and form a complex network. There are two B sites which are not included in any trimeron. More information on electronic structure is provided by *ab initio* calculations in Ref. [14].

Another *ab initio* calculation of electronic structure (using the hybrid Becke, three-parameter, Lee-Yang-Parr (B3LYP) exchange-correlation potential) was recently published by Patterson [15] together with an alternative description of Fe(B) charge ordering: Patterson focused on the ten shortest Fe(B)-Fe(B) bonds of bimodal distribution of Fe(B)-Fe(B) distances; part of these bonds forms a branched broken zigzag chain with delocalized minority-spin $3d$ electrons, while the rest presents one-electron bonds between pairs of Fe(B). Note that in the context of the trimeron model, these ten Fe(B)-Fe(B) bonds are parts of trimerons.

Nuclear magnetic resonance (NMR) is an efficient tool to study the inhomogeneous electron distribution locally. The analysis of the temperature dependence of ^{57}Fe NMR frequency in magnetite [16,17] evidenced the Cc space group of the Fe_3O_4 low-temperature crystal structure. The spectra acquired without an external magnetic field consisted of 16 Fe(B) and 8 Fe(A) resonance lines.

More than 10 years ago, Mizoguchi [18] succeeded in measuring the dependence of NMR frequencies on the direction of the external magnetic field. The data contain important information on the orbital state of individual Fe ions. However, the interpretation of such an experiment, in which magnetization lies in a general direction, is extremely difficult: the resonance lines are split due to the nature of *ac*-glide symmetry and also due to the presence of different elastic domains. At that time, the knowledge of the magnetite low-temperature crystal structure was far from complete, and the analysis of the results did not match the uniqueness of the experimental results.

Our work comprises a rigorous quantitative reanalysis of the experimental data of Mizoguchi. Although Patterson [15]

*reznicek@mbox.troja.mff.cuni.cz

also compared the calculated hyperfine field of iron ions to the data of Mizoguchi, there are important differences between his study and ours, which are explained in Secs. IV and V. We treat the presence of monoclinic twins and noncolinearity of the external magnetic field and magnetization properly, and our fits yield hyperfine anisotropy tensors and isotropic parts. Further, we calculate the electronic structure using the density functional theory (DFT) based WIEN2K program, with the main goal to determine the hyperfine field on the ^{57}Fe nuclei, including its anisotropy. We include the spin-orbit coupling in the calculation and focus on a proper calculation of the hyperfine field. The benefits of comparing experimental and calculated hyperfine field anisotropies were already clearly demonstrated in Ref. [19]. The results then allow us to assess the trimeron model validity.

II. TWINNING BELOW THE VERWEY TEMPERATURE

During cooling through the Verwey transition, the main deformation of magnetite structure is orthorhombic with orthogonal coordinates \vec{a} , \vec{b} , \vec{c}_0 . The \vec{c}_0 axis would be the easy magnetization direction, while \vec{a} is the hard direction. The lowering of symmetry from cubic to orthorhombic is accompanied by “orthorhombic” twinning; that is, below T_V , the crystal would consist of six types of orthorhombic domains. Mizoguchi applied an external magnetic field in a suitable direction during cooling to prevent orthorhombic twinning [18].

Simultaneously with orthorhombic deformation, a small monoclinic deformation occurs: the monoclinic axis \vec{c} is tilted from \vec{c}_0 by an angle 0.23° towards the $-\vec{a}$ axis. This small crystallographic deformation has a significant impact on magnetic anisotropy: the easy axis is not \vec{c}_0 , but it is canted by $\simeq 2^\circ$ towards $-\vec{a}$ [20]. There are two equivalent cantings, and accordingly, a monoclinic twinning exists. More details about the twinning are provided in the Supplemental Material [21].

III. ANGULAR DEPENDENCE OF THE NMR FREQUENCY

The frequency of the ^{57}Fe NMR resonance is proportional to the hyperfine magnetic field on the site of the resonating nucleus by a gyromagnetic factor $\gamma = 1.38156 \text{ MHz T}^{-1}$ [22]. The dependence of the NMR frequency f on the direction of \vec{M} is expressed using the direction cosines ϑ_α , $\alpha = a, b, c$ with respect to the orthorhombic \vec{a} , \vec{b} , \vec{c}_0 axes as

$$\begin{aligned} f &= f_{\text{iso}} + \begin{pmatrix} \vartheta_a \\ \vartheta_b \\ \vartheta_c \end{pmatrix} \begin{pmatrix} f_{aa} & f_{ab} & f_{ac} \\ f_{ab} & f_{bb} & f_{bc} \\ f_{ac} & f_{bc} & f_{cc} \end{pmatrix} \begin{pmatrix} \vartheta_a \\ \vartheta_b \\ \vartheta_c \end{pmatrix} \\ &= f_{\text{iso}} + \begin{pmatrix} \vartheta_a \\ \vartheta_b \\ \vartheta_c \end{pmatrix} \hat{F}_{\text{ani}} \begin{pmatrix} \vartheta_a \\ \vartheta_b \\ \vartheta_c \end{pmatrix}, \end{aligned} \quad (1)$$

which explicitly contains a constant isotropic term f_{iso} and anisotropy tensor \hat{F}_{ani} ($\text{Tr}[\hat{F}_{\text{ani}}] = 0$). (The fourth- and higher-order terms in the direction cosines are neglected.) The tensor of anisotropy can be brought to the canonical form

$$\hat{F}'_{\text{ani}} = \begin{pmatrix} f'_a & 0 & 0 \\ 0 & f'_b & 0 \\ 0 & 0 & f'_c \end{pmatrix}, \quad (2)$$

while at the same time obtaining principal axes \vec{p}_a , \vec{p}_b , and \vec{p}_c of the tensor. The following parameter can be defined as a measure of hyperfine anisotropy:

$$f_{\text{ani}} = \sqrt{f_a'^2 + f_b'^2 + f_c'^2} \quad (3)$$

In Cc symmetry, 16 sites from 32 Fe(B) are crystallographically inequivalent, and 8 sites from 16 Fe(A) are inequivalent. The symmetry operation that connects B_i, B'_i (A_i, A'_i) is represented by a glide along the \vec{c} axis with the ac -glide plane. Due to the symmetry, the parameter f_{ac} is the same for the two crystallographically equivalent sites, while the parameters f_{ab} , f_{bc} have opposite signs.

IV. REEVALUATION OF THE NMR DATA OF MIZOGUCHI

Mizoguchi measured the angular dependence of the NMR frequency of all inequivalent Fe nuclei in the low-symmetry phase of magnetite [18]. At 4.2 K, an external field $B_{\text{ext}} = 1.3 \text{ T}$ was rotated in the planes perpendicular to the orthorhombic \vec{a} , \vec{b} , \vec{c}_0 axes of a spherical sample in 10° steps. Thus 48 $f(B_{\text{ext}})$ curves were obtained: 16 for Fe on the A sites and 32 for Fe on the B sites. The splitting of the curves for magnetic field in the ac plane is due to monoclinic twinning, while the splitting for magnetization in the ab and bc planes is caused by the nature of the ac -glide symmetry (see Sec. III).

In order to analyze the experimental data, the noncolinearity of \vec{M} and \vec{B}_{ext} must be accounted for. To this end, we employed a procedure similar to the one used by Mizoguchi [23]: the direction of the magnetization in \vec{B}_{ext} was numerically determined using the magnetic anisotropy reported originally by Abe *et al.* [20] (see the Supplemental Material [21]). (Note that in the analysis in Ref. [15], the presence of monoclinic twins and noncolinearity of the external magnetic field and magnetization in the sample were neglected; their effect was mentioned only in discussion.)

The frequency shift induced by the external field was compensated for by subtracting a projection of \vec{B}_{ext} onto the \vec{M} direction (multiplied by γ) from the data. Next, the data were fitted with the dependence (1) while taking into account the splitting of the curves for each Fe site. Typical errors of the fitted parameters were below or around 0.01 MHz for the A sites and 0.02–0.7 MHz for the B sites. Finally, the canonical form of the \hat{F}_{ani} tensor was found. The results are listed in Table S1 in the Supplemental Material [21], and fitted curves are plotted in Fig. 1. The fitted frequency dependences match the experimental data well, showing that the truncation of the fourth-order terms in Eq. (1) is well founded. Unfortunately, a comparison of these results with the work of Patterson [15] is not feasible since the isotropic parts and anisotropy tensors of the hyperfine field were not extracted from the calculated and experimental data in his work.

V. CALCULATION OF THE ELECTRONIC STRUCTURE AND HYPERFINE FIELD

To calculate the hyperfine field as well as the electronic structure, the WIEN2K program [24] based on the density functional theory was used. The number of basis functions used was 9500 ($\text{RK}_{\text{max}} = 6.0$), and the number of k points in

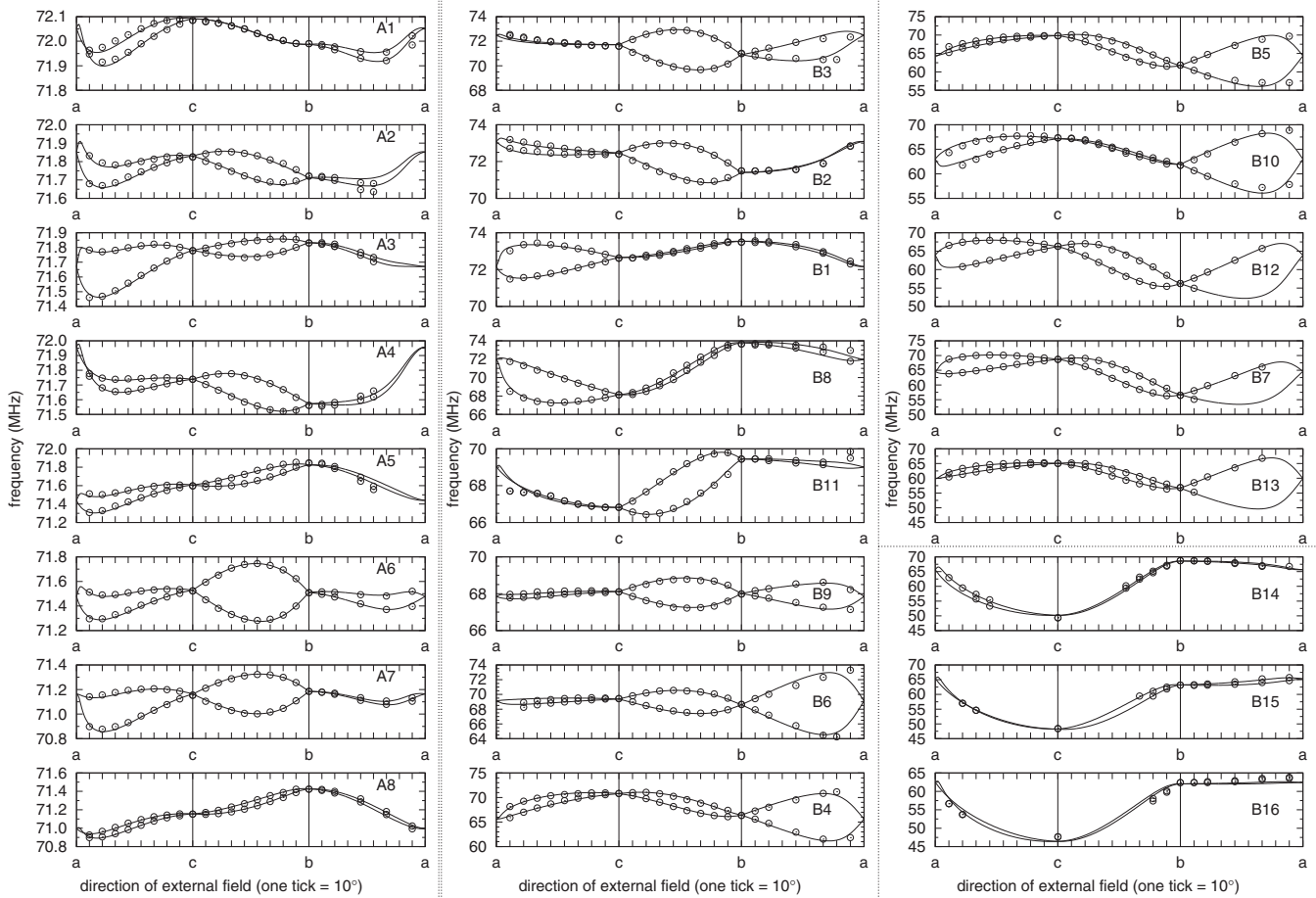


FIG. 1. Angular dependence of ^{57}Fe NMR frequencies with $H_{\text{ext}} = 1.3$ T applied in the ac , bc , and ab planes. Circles correspond to the experimental data [18], and curves represent the best fit of Eq. (1) to these data. The labels of the sites follow the convention in Ref. [18]. Ordering of the B sites corresponds to the ordering in Table S3 and Fig. S4 in the Supplemental Material [21].

the irreducible part of the Brillouin zone was 9. The charge density was Fourier expanded to $G_{\text{max}} = 16 \text{ Ry}^{\frac{1}{2}}$.

The crystal structure parameters used were those published by Senn *et al.* [10] for the low-temperature phase of magnetite. While Patterson [15] optimized the structure, we decided to avoid the optimization process because the structure is complicated and a number of crystal-structure parameters would change during the optimization. Necessarily, multiple total-energy minima exist, and there is no guarantee that the correct minimum would be reached. Moreover, the situation is complicated by magnetostriction, which is not taken into account in the optimization procedure. Therefore we decided to use the unoptimized experimental structure, in which the average force acting on the ions was $9.8 \text{ mRy a.u.}^{-1}$ and the maximum force was $19.3 \text{ mRy a.u.}^{-1}$.

The contact part of the hyperfine field was calculated using a semiempirical method suggested recently by Novák and Chlan [25], which is better than the approach used in Ref. [15] as the corresponding Eq. (3) in Ref. [15] is a poor approximation of the contact term [26]. To this end, the spin magnetic moments m_{3d} and m_{4s} of the $3d$ and $4s$ electrons of Fe are needed. These were calculated using $R_{\text{MT}}(\text{Fe}) = 2 \text{ a.u.}$ and the generalized gradient approximation $+U$ (GGA $+U$) method, with $U_{\text{eff}} = 4.5 \text{ eV}$. Unlike in Ref. [14], spin-orbit coupling was not omitted. The on-site contributions to the hyperfine

field from the interaction of nuclear spin with the electron spin (B_{dip}) and orbital moment (B_{orb}) were calculated as described in Ref. [25], and the contribution of other magnetic moments in the lattice B_{lat} was also calculated. For the iron ions at the B sites, $|B_{\text{dip}}|$ ranges up to 13.7 T, $|B_{\text{orb}}|$ ranges up to 4.6 T, $|B_{\text{lat}}|$ ranges up to 1.1 T, and the anisotropy of all of these terms is significant. (In Ref. [15], the terms corresponding to the interaction of nuclear spin with orbital moments and with electron magnetic moments on other sites are missing.) The total hyperfine field was then obtained by summing up all components.

A. Valence-electron density in trimeron planes

One of the ways in which the DFT calculations may contribute to the understanding of the trimeron concept [10] is maps of minority-spin valence-electron density in selected planes of the trimerons (see Fig. 2; see also Fig. S2 in the Supplemental Material [21], which is limited to minority-spin iron $3d$ valence electrons). The electron density is calculated for the magnetization set in the \vec{c} axis, and the maps are plotted as averages of the ac -glide-connected sites to remove possible (although minor) artifacts arising from switching off this symmetry operation in order to be consistent with calculations of the angular dependences. The main finding is that the electron cloud around the central Fe^{2+} -like ion of each

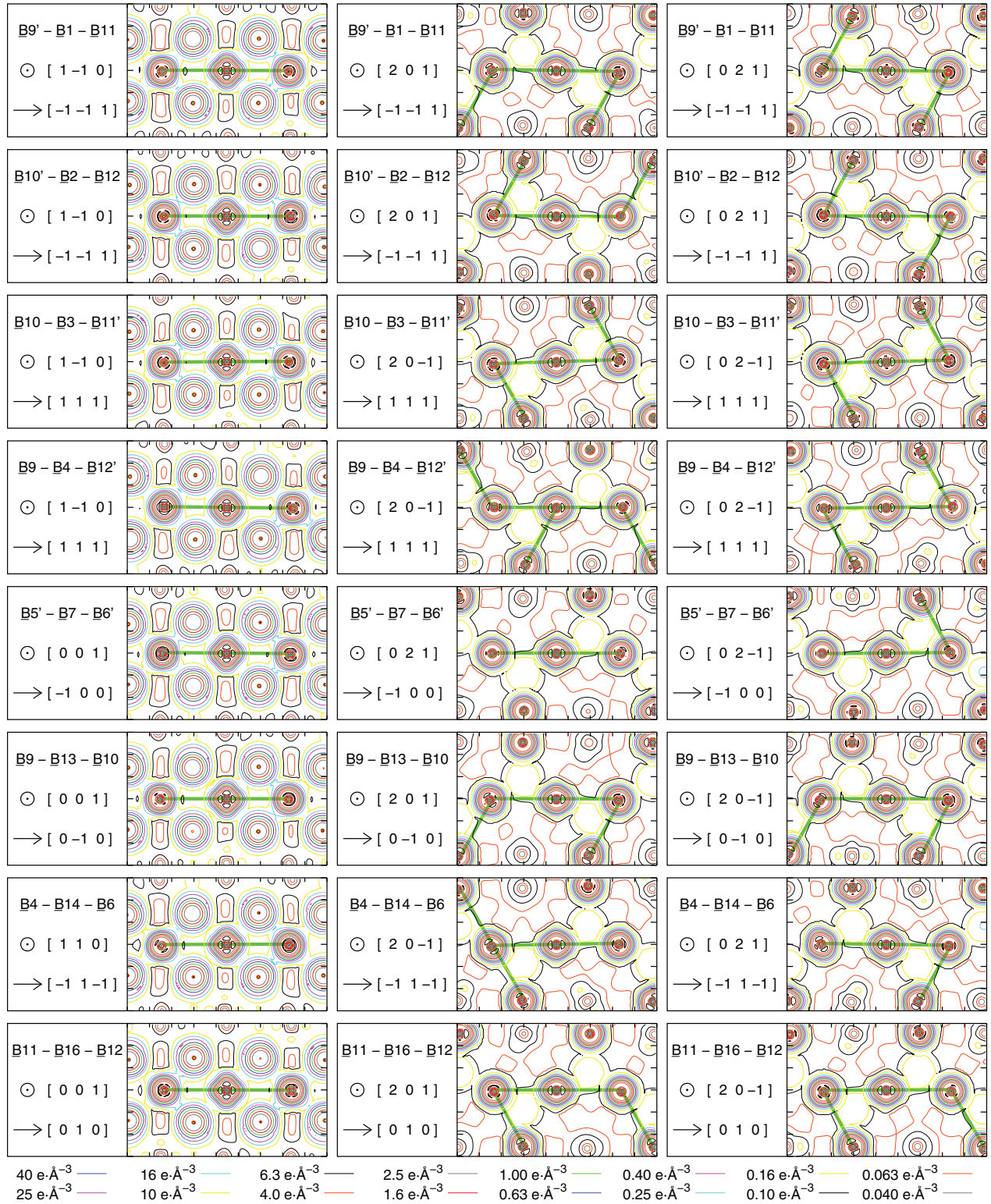


FIG. 2. (Color) Minority-spin valence-electron-density maps plotted in trimeron planes. The size of each plot is $9 \times 6 \text{ \AA}$. Trimerons [10] are highlighted with green lines. The sites of iron ions forming the trimeron lying on a horizontal axis of a particular plot are written on each plot; the center of the image plane coincides with the position of the central ion of the trimeron. Since the \vec{c} axis tilt in the monoclinic Cc cell of magnetite renders the standard crystallographic plane notation inconvenient for selected planes, the orientation of the planes is indicated by the normal vector of the plane (pointing out of the image) written at the circled dot symbol and by an in-plane vector drawn by an arrow; indices of these vectors refer to Cc coordinates. The planes in the first column form with the other two planes in a corresponding row an angle of $\approx 55^\circ$, while the latter planes make together an angle of $\approx 70.5^\circ$. Sites are numbered in the order in which they are listed in Ref. [10]; primes denote sites generated by the ac -glide symmetry operation.

TABLE I. Minority-spin electron populations relative to Fe^{3+} , as derived from [10] (first line) and from the DFT calculations (second line), accompanied by formal valence and oxidation states (in units of electron charge) and magnetic moments (in Bohr magnetons) from the AIM method. The n_{3d} populations taken from [15] correspond to 16 bands just below the valence-band maximum. Sites are numbered in the order in which they are listed in Ref. [10]. Populations are taken with respect to local coordinates with the \vec{z} axis parallel to the \vec{c} axis of the Cc system and the \vec{x} axis set to the [110] direction with respect to the Cc coordinates. For the A sites, the AIM yielded valences of 1.77 (i.e., oxidation states of 2.82) and magnetic moments in the range from -4.079 to -4.095 .

DFT site	Nominal valence state										AIM	AIM oxidation	AIM spin
		n_{xy}	n_{xz}	n_{yz}	$n_{t_{2g}}$	n_{z^2}	$n_{x^2-y^2}$	n_{e_g}	$n_{t_{2g}} + n_{e_g}$	n_{3d} [15]	valence	state	magnetic moment
<u>B1</u>	2+	0.00	0.60	0.00	0.60	0.00	0.00	0.00	0.60				
		0.03	0.73	0.04	0.80	0.10	0.11	0.21	1.01	0.63	1.47	2.34	3.691
<u>B2</u>	2+	0.00	0.60	0.00	0.60	0.00	0.00	0.00	0.60				
		0.03	0.74	0.04	0.80	0.09	0.11	0.20	1.01	0.61	1.46	2.33	3.696
<u>B3</u>	2+	0.00	0.60	0.00	0.60	0.00	0.00	0.00	0.60				
		0.03	0.70	0.05	0.78	0.10	0.11	0.21	0.99	0.65	1.47	2.35	3.708
<u>B4</u>	2+	0.00	0.60	0.20	0.80	0.00	0.00	0.00	0.80				
		0.03	0.55	0.05	0.63	0.12	0.13	0.25	0.88	0.48	1.57	2.51	3.858
<u>B5</u>	3+	0.20	0.00	0.00	0.20	0.00	0.00	0.00	0.20				
		0.12	0.07	0.06	0.25	0.21	0.19	0.40	0.65	0.29	1.79	2.85	4.153
<u>B6</u>	3+	0.20	0.00	0.20	0.40	0.00	0.00	0.00	0.40				
		0.09	0.05	0.19	0.33	0.18	0.18	0.36	0.69	0.39	1.74	2.78	4.095
<u>B7</u>	2+	0.60	0.00	0.00	0.60	0.00	0.00	0.00	0.60				
		0.72	0.03	0.03	0.78	0.12	0.09	0.21	0.99	0.53	1.48	2.36	3.722
<u>B8</u>	3+	0.00	0.00	0.00	0.00	0.00	0.00	0.00	0.00				
		0.07	0.06	0.06	0.20	0.22	0.21	0.43	0.62	0.07	1.83	2.92	4.192
<u>B9</u>	3+	0.20	0.20	0.20	0.60	0.00	0.00	0.00	0.60				
		0.05	0.31	0.07	0.43	0.15	0.17	0.32	0.75	0.44	1.68	2.68	4.021
<u>B10</u>	3+	0.20	0.20	0.20	0.60	0.00	0.00	0.00	0.60				
		0.13	0.11	0.11	0.34	0.18	0.18	0.36	0.70	0.45	1.73	2.76	4.081
<u>B11</u>	3+	0.20	0.20	0.20	0.60	0.00	0.00	0.00	0.60				
		0.11	0.13	0.12	0.36	0.18	0.18	0.35	0.71	0.45	1.72	2.74	4.066
<u>B12</u>	3+	0.20	0.20	0.20	0.60	0.00	0.00	0.00	0.60				
		0.08	0.09	0.07	0.25	0.20	0.20	0.41	0.65	0.26	1.79	2.86	4.146
<u>B13</u>	2+	0.60	0.00	0.00	0.60	0.00	0.00	0.00	0.60				
		0.76	0.03	0.03	0.81	0.12	0.09	0.20	1.01	0.60	1.46	2.33	3.692
<u>B14</u>	2+	0.00	0.00	0.60	0.60	0.00	0.00	0.00	0.60				
		0.03	0.03	0.69	0.76	0.10	0.12	0.22	0.97	0.52	1.50	2.39	3.736
<u>B15</u>	3+	0.00	0.00	0.00	0.00	0.00	0.00	0.00	0.00				
		0.07	0.06	0.06	0.19	0.21	0.21	0.42	0.62	0.07	1.83	2.92	4.195
<u>B16</u>	2+	0.60	0.00	0.00	0.60	0.00	0.00	0.00	0.60				
		0.75	0.03	0.03	0.80	0.12	0.08	0.20	1.00	0.64	1.46	2.32	3.703

trimeron is notably prolate along the trimeron axis. Moreover, the asymmetry of the electron density around the end ions of trimerons is smaller and, in some cases, negligible.

The observations correspond well to the picture of trimerons: a significant fraction of minority-spin $3d$ electron is located in that central ion's t_{2g} orbital which corresponds to the trimeron axis direction, while the rest of the electron is donated to the same orbitals of the end ions. Therefore the electron density around the central ion is considerably anisotropic. The symmetry of the electron clouds around the end ions is affected much less even if the ion belongs to more than one trimeron as the donated fractional charges enter different orbitals in such a case.

The comparison of the data with the model of Patterson [15] is less plausible: While the description above might fulfill the expectations for inner ions of the zigzag chain, a shift of the electron cloud towards the chain would be intuitively presumed

in the case of the chain end or branch ions (e.g., B1, B13), which is not observed. The expected situation for the Fe(B) pairs not included in the chain (e.g., B5'–B7) also differs from the maps.

B. Electron populations and valence states of iron on the B sites

The description of trimerons in Ref. [10] allows us to determine qualitatively the populations of the iron minority-spin $3d$ states; that is, assuming maximum donor-to-acceptor transfer, $0.6e$ (e stands for elementary charge) remains in the central ion's t_{2g} orbital which corresponds to the trimeron axis direction, while $0.2e$ is donated to the same orbital of each of the end ions. These populations are compared with the results of the DFT calculation in Table I. [These populations are taken with respect to orthogonal coordinates reflecting local (pseudo)symmetry: the \vec{z} axis parallel to \vec{c} , the \vec{x} axis

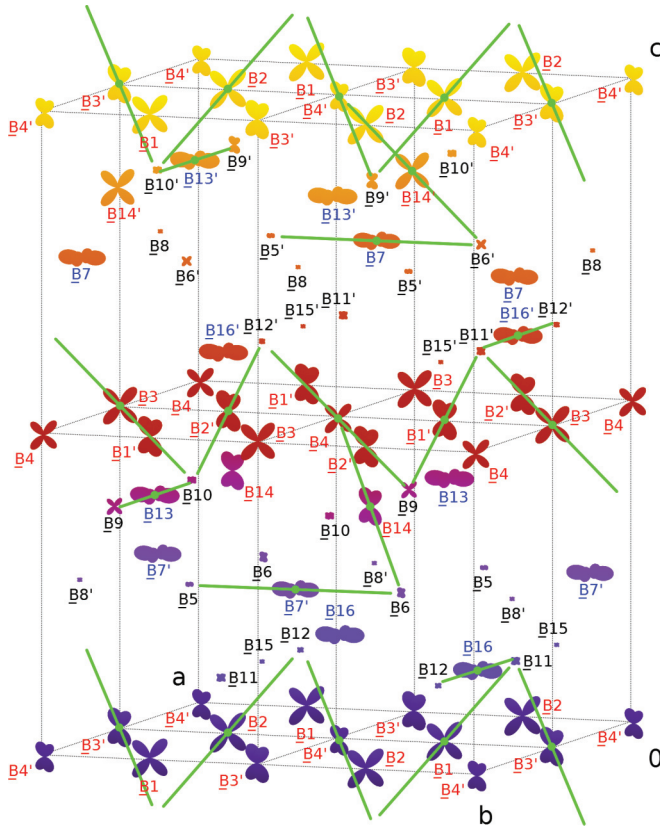


FIG. 3. (Color) Minority-spin t_{2g} electron populations of iron ions at the B sites plotted as an angular variation of the electron density; that is, the surface distance from a particular site represents the density at the corresponding angle multiplied by a scaling coefficient of 3 \AA^{-1} . Green lines denote trimerons introduced in Ref. [10]. Sites are numbered in the order in which they are listed in Ref. [10]; primes denote sites generated by the ac -glide symmetry operation. Sites in the same group in Fig. S4 in the Supplemental Material [21] share the same label color. (Surface color corresponds to the z coordinate and is used just for clarity.)

along the $[110] Cc$ direction.] The populations obtained from the DFT calculation are visualized in Fig. 3 [27], and it is seen that the calculation results correlate well with the expected t_{2g} populations. Mulliken populations of minority-spin $3d$ electrons from Ref. [15] were added to Table I for a comparison (note that these populations correspond to 16 bands just below the valence-band maximum, whereas there was no additional energy or band restriction of the $3d$ orbitals applied in our data); the apparent correlation to our data and trimeron model predictions is interesting. Concerning the valence of the B irons, the sums of t_{2g} and e_g spin-down electron densities of Fe^{2+} -like ions are close to 1, while they are systematically lower for Fe^{3+} -like ions, although still significantly higher than zero. The total number of these electrons yields 13.25 electrons at the 16 B sites, while only 8.00 electrons are expected if, formally, eight divalent and eight trivalent iron ions occupy these sites. The surplus 5.25 electrons are transferred from oxygen ligands. In order to reliably quantify the valence states of the B sites, atomic valences, oxidation states, and also magnetic moments were determined using the atoms in molecules (AIM) method [28] (see the last three columns in

Table I). In order to obtain oxidation states, the valence charges calculated from AIM were rescaled by a factor of 1.6, which brings the average valence charge of oxygen ions to -2 , thus representing the oxidation state O^{2-} . The resulting B iron valence states correlate very well with the bond valence sum (BVS) values reported in Ref. [10].

C. Hyperfine field anisotropy

Complementary to Mizoguchi's experiments [18], the DFT calculations of the hyperfine field at iron sites were carried out for various directions of magnetization and subsequently fitted with Eq. (1). Typical uncertainty of the fitted parameters was smaller than 0.03 MHz for the A sites and 0.03–0.6 MHz for the B sites. The results are collected in Table S2 in the Supplemental Material [21], and fitted curves are drawn in Fig. 4. Note the difference that Mizoguchi rotated the external magnetic field in the ac , cb , and ab planes, while in our calculations it was the magnetization that was rotated in these planes.

The DFT calculations performed for magnetization not parallel to the easy axis have two limitations. First, for a general specified magnetization direction, the spin and orbital magnetization tends to incline towards the easy magnetization axis due to the spin-orbit coupling. In the case of our calculations, the resulting direction of total magnetization (which entered then into the fit) deflected from the specified direction for not more than 10° , and the magnetic moments of individual iron ions were collinear, as expected (deviations from the total magnetization direction were less than 0.5°). Second, the complex dependence of the total energy on the magnetization direction is likely to possess multiple local minima. Therefore, the self-consistent iteration procedure for neighboring (or even the same) magnetization directions may be prone to converge to unrelated minima depending on the population matrices with which the GGA+ U calculation was started. In order to estimate the impact of this effect, the calculations for the specified magnetization direction $[30\bar{1}]$ were carried out independently twice, and the determined error of the hyperfine field was up to 0.3 T (i.e., 0.4 MHz error of the ^{57}Fe NMR frequency).

The hyperfine anisotropy tensors \hat{F}_{ani} of $\text{Fe}(\text{B})$ ions are visualized in Fig. 5 as objects drawn in the elementary cell; the following formula defines the distance r of the object surface from the particular iron position:

$$r = C [f_{aa}\vartheta_a^2 + f_{bb}\vartheta_b^2 + f_{cc}\vartheta_c^2 + 2(f_{ab}\vartheta_a\vartheta_b + f_{ac}\vartheta_a\vartheta_c + f_{bc}\vartheta_b\vartheta_c)], \quad (4)$$

where ϑ_α , $\alpha = a, b, c$, are direction cosines taken relative to the iron site in question and C is a scaling coefficient common for all B sites, allowing for a clear drawing. Figure 5 provides an overview of mutual orientation of principal axes of hyperfine anisotropy tensors of neighboring $\text{Fe}(\text{B})$ ions, which can be compared to the concept of trimerons suggested by Senn *et al.* [10]. The trimerons are depicted in Fig. 5 by the line segments in the center of which the Fe^{2+} -like ions are situated. Apparently, the trimeron central ions exhibit considerably larger anisotropy than the end ions, while the principal axis linked with the smallest eigenvalue of the

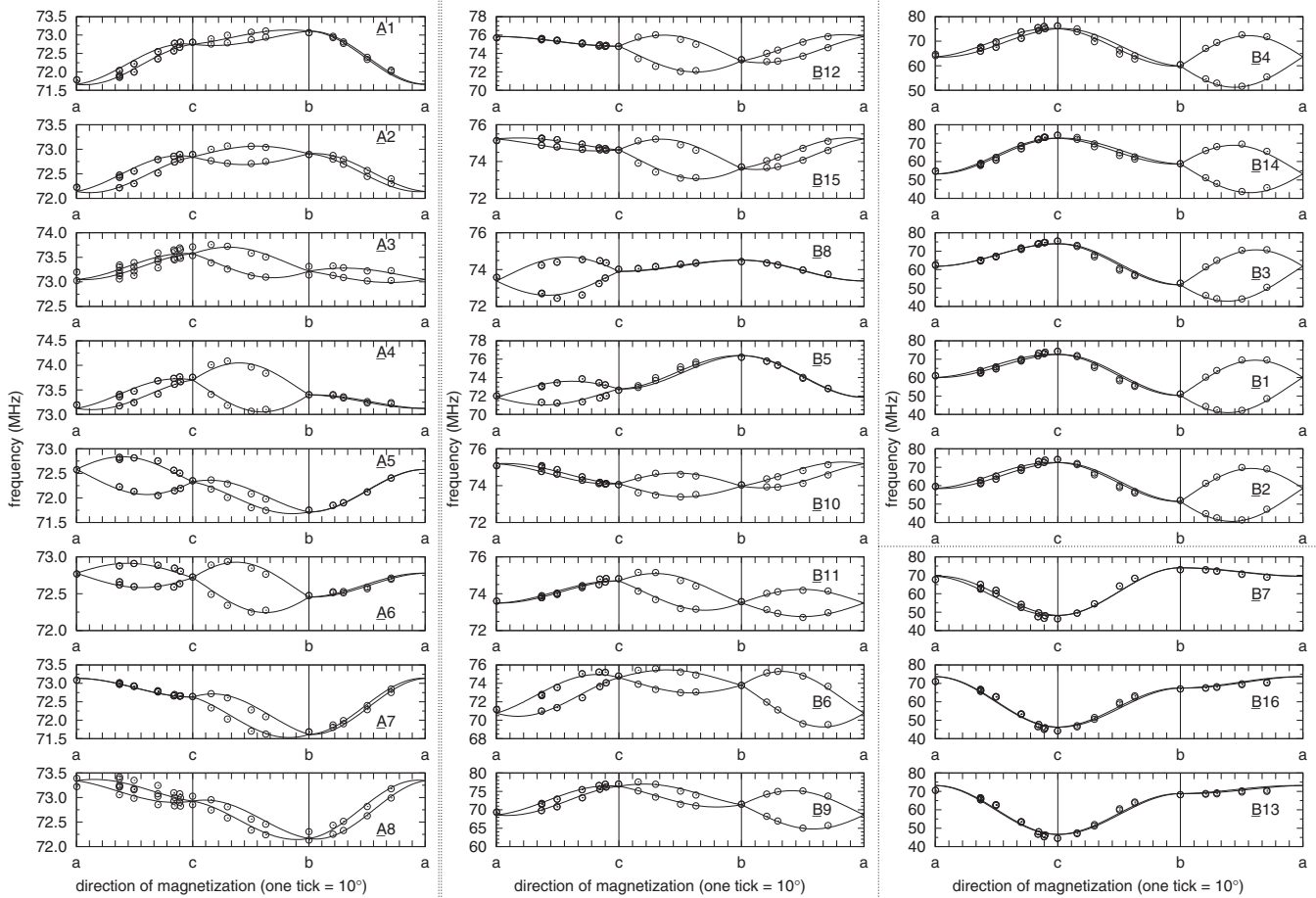


FIG. 4. Angular dependence of ^{57}Fe NMR frequencies with magnetization in the ac , bc , and ab planes. Circles correspond to the data from the DFT calculations, and curves represent the best fit of Eq. (1) to these data. Sites are numbered in the order in which they are listed in Ref. [10]. Ordering of the B sites corresponds to the ordering in Table S3 and Fig. S4 in the Supplemental Material [21].

corresponding anisotropy tensor of the central ion is the closest to the trimeron axis. These findings are in agreement with the expectations deduced from the electronic structure of trimerons: The minority-spin charge density around the central Fe^{2+} -like ions is significantly anisotropic as the charge is located in a t_{2g} orbital corresponding to the trimeron axis. On the other hand, the roughly spherical symmetry of the Fe^{3+} -like end ions is affected only by the partial charge donated by the central ions. (If the end ion is a member of multiple trimerons, the central ions donate the charge into different orbitals; thus the impact on the end-ion symmetry remains small.) In the case of Fe^{3+} -like ions **B8** and **B15**, which do not belong to any trimeron, the anisotropy is small as their symmetry is not significantly perturbed. We note that the model proposed by Patterson [15] implies a similar charge configuration of the two iron ions in the pairs that are not in the zigzag chain (e. g. **B5'**–**B7**). This is not corroborated by our calculations as their anisotropies are apparently different. For a visualization of the significantly smaller anisotropy tensors of Fe(A) ions, see Fig. S3 in the Supplemental Material [21]. The small anisotropy of the Fe^{3+} ions at the A sites corresponds to nearly spherical symmetry of their electronic configuration.

VI. COMPARISON OF THE HYPERFINE PARAMETERS EXTRACTED FROM THE NMR DATA AND FROM THE DFT CALCULATIONS

A simple way to compare experimental and calculated NMR frequencies of Fe(B) ions is displayed in Fig. 6. In this figure, the frequencies are ordered according to their decreasing isotropic part f_{iso} , and it is seen that both data sets can be divided into two groups. Fe ions in the left part of the plot possess smaller anisotropy f_{ani} and higher f_{iso} compared to Fe in the right part. This is understandable: The iron ions in the first group are Fe^{3+} -like (see Table I), and as a consequence, they have a small orbital moment, and thus anisotropy is also small. At the same time, the occupation of the minority-spin $3d$ states is small, leading to higher spin moment and, consequently, also a higher isotropic part of the NMR frequency. The interpretation of the experimental hyperfine parameters in the context of the trimeron electronic structure is essentially the same as that provided in Sec. V C.

Closer correlation of experimental and calculated NMR frequencies may be obtained by considering both f_{iso} and the anisotropy tensor \hat{F}_{ani} . To this end, we calculate the mean

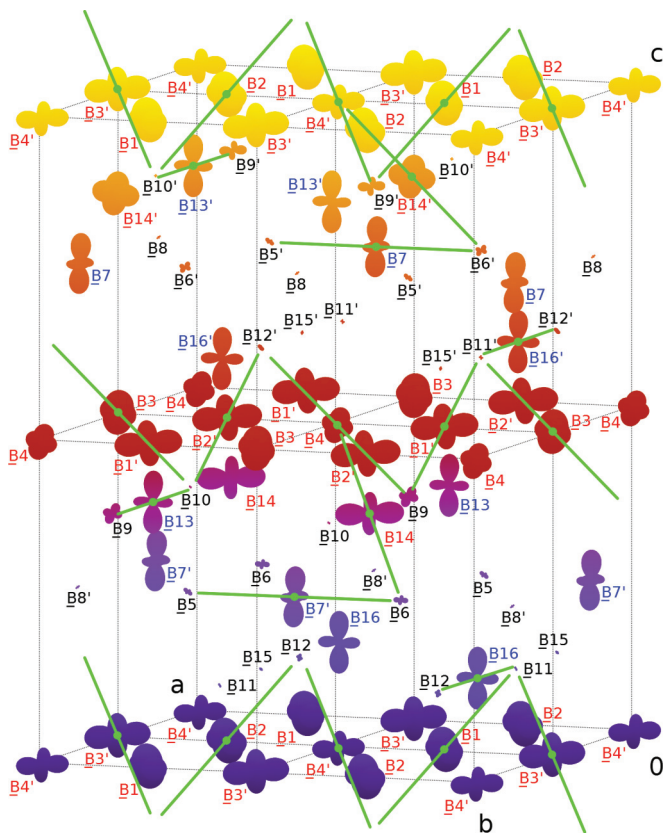


FIG. 5. (Color) Tensors of hyperfine anisotropy of iron B sites from the DFT calculations drawn in the elementary cell (scaling coefficient $C = 0.05 \text{ \AA MHz}^{-1}$). Green line segments correspond to trimerons suggested in Ref. [10]. Sites are numbered in the order in which they are listed in Ref. [10]; primes denote sites generated by the ac -glide symmetry operation. Sites in the same group in Fig. S4 in the Supplemental Material [21] share the same label color. (Surface color corresponds to the z coordinate and is used just for clarity.)

square deviation $\sigma(i, j)$:

$$\sigma(i, j) = \left(\sum_{\alpha=aa, bb, cc} \{ [f_{\text{iso}}^{\text{calc}}(i) + f_{\alpha}^{\text{calc}}(i)] - [f_{\text{iso}}^{\text{exp}}(j) + f_{\alpha}^{\text{exp}}(j)] \}^2 + 2 \sum_{\alpha=ab, ac, bc} [f_{\alpha}^{\text{calc}}(i) - f_{\alpha}^{\text{exp}}(j)]^2 \right)^{1/2}. \quad (5)$$

The index i of the calculated data corresponds to a specific B site in the unit cell, while for the experimental data the index j corresponds to a particular pair of branches of angular dependence of the NMR frequency. (The f_{ab} and f_{bc} elements obtained from experimental data have an arbitrary sign, whereas the sign of their product is known. Considering this, the variants of the signs resulting in the smallest $\sigma(i, j)$ were chosen for the calculation.) The $\sigma(i, j)$ then helps us to associate the B sites and the hyperfine field experimentally observed. The values of $\sigma(i, j)$ determined using the above equation are collected in Table S3 in the Supplemental Material [21]. Total mean-square deviation

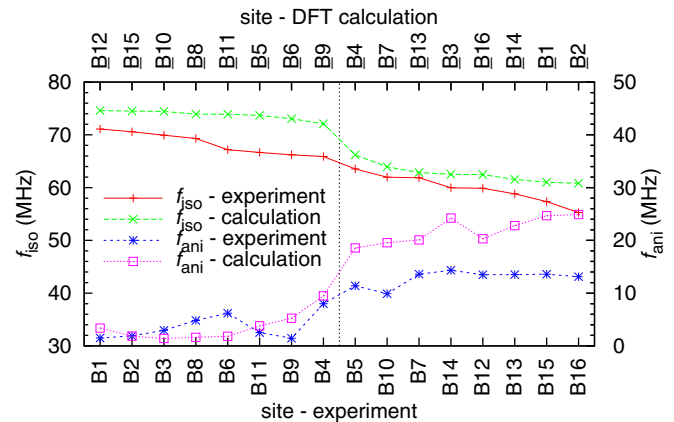


FIG. 6. (Color online) Comparison of the anisotropic and isotropic parts of the NMR frequencies extracted from the experimental data of Mizoguchi and from the DFT calculations. The B sites are ordered by decreasing f_{iso} . For experimental data, the labels of the sites follow the convention in Ref. [18]. For the DFT results, the sites are numbered in the order in which they are listed in Ref. [10].

for each assignment of calculated and experimental data is obtained by summing $\sigma(i, j)$:

$$\sigma = \frac{1}{16} \sum_{K=1}^{16} \sigma(i_K, j_K). \quad (6)$$

The 16 pairs (i_K, j_K) of indices are fixed by selecting the assignment. The minimal value of σ is $\sigma_{\text{min}} = 11 \text{ MHz}$. One of the best assignments (the diagonal of Fig. S4 in the Supplemental Material [21]) is plotted in Fig. 7 in the same way as for Fig. 5. We note, however, that there exist several assignments with σ close to σ_{min} .

Inspection of the results revealed three groups (in 8:5:3 ratio) of B sites in which the parameters of experimental and DFT data correlate. These groups are marked by label colors in Figs. 3, 5, and 7. The first group contains eight Fe^{3+} -like ions exhibiting lower anisotropy, confirming the observation from Fig. 6. Moreover, the procedure successfully identified the three NMR signals which are separated at low frequencies from the rest of a zero-field spectrum [16,17] with a group of three crystallographic sites with similar tensors of anisotropy; the longest principal axis of the tensors points along the \vec{c}_0 axis, while the other two principal axes are close to the \vec{a} and \vec{b} directions. The five Fe^{2+} -like ions in the remaining group are located approximately in $\{002\}$ planes of the Cc cell, with the exception of the B14 iron ion, and the principal axis of the anisotropy tensor corresponding to the largest (in absolute value) eigenvalue is not far from either the $[110]$ or $[1\bar{1}0]$ direction (with respect to Cc coordinates).

Hyperfine anisotropy of Fe^{3+} at the A sites is small, and also the isotropic terms differ only slightly. For these reasons we did not attempt to correlate the calculated and experimental data.

VII. CONCLUSIONS

We succeeded in quantitatively reanalyzing Mizoguchi's measurements of the angular dependences of the ^{57}Fe NMR

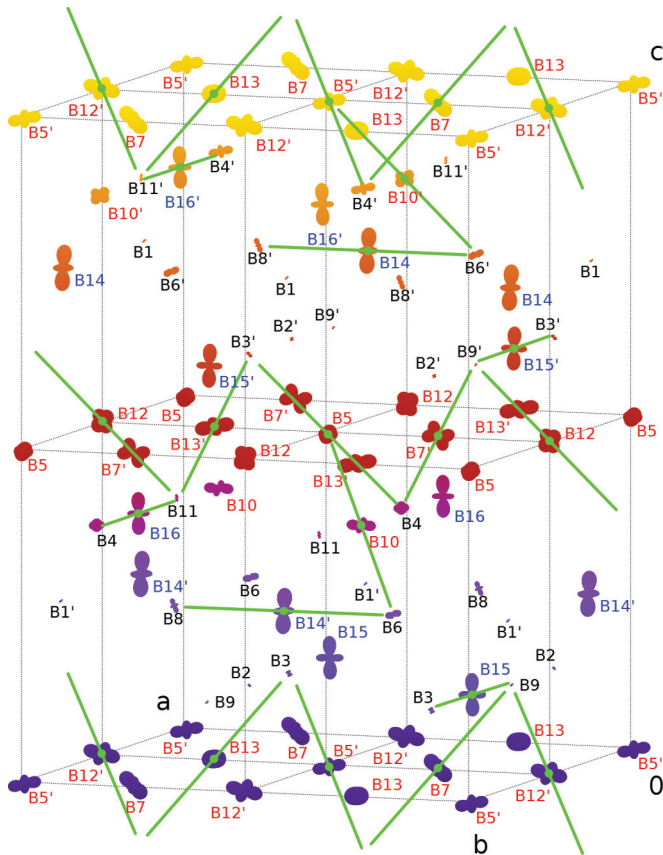


FIG. 7. (Color) Tensors of the anisotropy of iron B sites from the NMR data drawn in the elementary cell (scaling coefficient $C = 0.05 \text{ \AA MHz}^{-1}$). The assignment with one of the minimal total mean-square deviations σ (6) is plotted. Green lines denote trimerons as suggested in Ref. [10]. The labels of the sites follow the convention in Ref. [18]; primes denote sites generated by the ac -glide symmetry operation. Sites in the same group in Fig. S4 in the Supplemental Material [21] share the same label color. (Surface color corresponds to the z coordinate and is used just for clarity.)

frequencies [18] in the low-temperature phase of magnetite and extracted the isotropic parts and anisotropy tensors of the NMR frequency. These data are directly proportional to the isotropic parts and anisotropy tensors of the hyperfine field. Moreover, we performed the DFT calculations of the hyperfine field dependence on the magnetization direction using the crystal structure reported by Senn *et al.* [10] and evaluated the results in order to obtain analogous anisotropy data linked to particular crystallographic sites. These two sets of data were compared, and although a reliable unique assignment of NMR lines to crystallographic sites was not feasible, three mutually

matching groups of B sites in a ratio of 8:5:3 were found. The first group is occupied by the Fe^{3+} -like ions; the other ones are occupied by the Fe^{2+} -like ions. This grouping allows one to narrow down the range of B sites a particular NMR signal may originate from and also supports the validity of the calculations and the underlying crystal structure as the B-site data sets from the DFT calculations share the same grouping ratio as the ones from the experiment.

Further, the hyperfine anisotropy data obtained from the DFT calculations support the trimeron concept [10] as the central Fe^{2+} -like ions of the suggested trimerons exhibit significantly larger anisotropy than the end ions and the principal axis linked with the smallest eigenvalue of the corresponding anisotropy tensor of the central ions is the closest to the trimeron axis, which is in agreement with expectations deduced from the description of the electron distribution in the trimerons. Even more direct insight into the electronic ordering of the trimerons can be found in the calculated maps of minority-spin valence-electron density, which indicate that the electron cloud around the central ion of each trimeron is prolate along the trimeron axis.

Moreover, the minority-spin valence-electron populations at the B sites were acquired from the DFT calculations, and the AIM method was used to determine iron valences and magnetic moments. The populations were compared to the trimeron model, and the valences correlated to the BVS data [10], both showing good agreement.

Despite the discrepancies found between the approach of Patterson [15] and our results, we understand Patterson's model and the model of trimerons as alternative views on the same physical reality: Patterson's concept of the broken branched zigzag chain and pairs of Fe(B) ions with one-electron bonds coincides with the trimeron network without longer bonds. The $\text{Fe(B)}\text{-Fe(B)}$ distances present important information on which both models are based. However, imposing a strict limit on bond length between Fe(B) pairs to qualify for a charge transfer in Patterson's model does not seem appropriate as the bond length distribution is not wide, so the overlap of t_{2g} orbitals of neighboring Fe(B) ions is significant even if their distance is not so short. Therefore the trimeron model provides a more precise description of the electronic structure of magnetite, as was shown by our results.

ACKNOWLEDGMENTS

This study was supported by project SVV-2014-260091. The work is part of the activities of the Charles University Research Center UNCE 204023 "Physics of Condensed Matter and Functional Materials." Last but not least, the authors are grateful to J. Šváb and K. Uličná for extraction of the data points from the plots in Ref. [18].

- [1] V. A. M. Brabers, Progress in spinel ferrite research, in *Handbook of Magnetic Materials*, edited by K. H. J. Buschow, Vol. 8 (Elsevier, Amsterdam, 1995), pp. 189–234.
- [2] J. M. Honig, Analysis of the Verwey transition in magnetite, *J. Alloys Compd.* **229**, 24 (1995).

- [3] F. Walz, The Verwey transition—A topical review, *J. Phys. Condens. Matter* **14**, R285 (2002).
- [4] J. P. Wright, J. P. Attfield, and P. G. Radaelli, Charge ordered structure of magnetite Fe_3O_4 below the Verwey transition, *Phys. Rev. B* **66**, 214422 (2002).

- [5] J. García and G. Subías, The Verwey transition—A new perspective, *J. Phys. Condens. Matter* **16**, R145 (2004).
- [6] M. S. Senn, J. P. Wright, and J. P. Attfield, The Verwey Phase of Magnetite—A Long-Running Mystery in Magnetism, *J. Korean Phys. Soc.* **62**, 1372 (2013).
- [7] G. Subías, J. García, J. Blasco, J. Herrero-Martín, M. C. Sánchez, J. Orna, and L. Morellón, Structural distortion, charge modulation and local anisotropies in magnetite below the Verwey transition using resonant X-ray scattering, *J. Synchrotron Rad.* **19**, 159 (2012).
- [8] S.-Ch. Weng, Y.-R. Lee, Ch.-G. Chen, Ch.-H. Chu, Y.-L. Soo, and S.-L. Chang, Direct observation of charge ordering in magnetite using resonant multiwave X-Ray diffraction, *Phys. Rev. Lett.* **108**, 146404 (2012).
- [9] A. Tanaka *et al.*, Symmetry of Orbital Order in Fe₃O₄ Studied by Fe L_{2,3} Resonant X-Ray Diffraction, *Phys. Rev. Lett.* **108**, 227203 (2012).
- [10] M. S. Senn, J. P. Wright, and J. P. Attfield, Charge order and three-site distortions in the Verwey structure of magnetite, *Nature (London)* **481**, 173 (2012).
- [11] E. J. W. Verwey, Electronic Conduction of Magnetite (Fe₃O₄) and its Transition Point at Low Temperatures, *Nature (London)* **144**, 327 (1939).
- [12] A. Bosak, D. Chernyshov, M. Hoesch, P. Piekarczyk, M. Le Tacon, M. Krisch, A. Kozłowski, A. M. Oleś, and K. Parlinski, Short-range correlations in magnetite above the Verwey temperature, *Phys. Rev. X* **4**, 011040 (2014).
- [13] S. de Jong, R. Kukreja *et al.*, Speed limit of the insulator-metal transition in magnetite, *Nat. Mater.* **12**, 882 (2013).
- [14] M. S. Senn, I. Loa, J. P. Wright, and J. P. Attfield, Electronic orders in the Verwey structure of magnetite, *Phys. Rev. B* **85**, 125119 (2012).
- [15] C. H. Patterson, Hybrid DFT calculation of ⁵⁷Fe NMR resonances and orbital order in magnetite, *Phys. Rev. B* **90**, 075134 (2014).
- [16] P. Novák, H. Štěpánková, J. Englich, J. Kohout, and V. A. M. Brabers, NMR in magnetite below and around the Verwey transition, *Phys. Rev. B* **61**, 1256 (2000).
- [17] P. Novák, H. Štěpánková, J. Englich, J. Kohout, and V. A. M. Brabers, Temperature Dependence of NMR in Magnetite, in *Ferrites: proceedings of ICF 8, Kyoto and Tokyo, Japan 2000*, edited by M. Abe and Y. Yamazaki (Japan Society of Powder and Powder Metallurgy, Kyoto and Tokyo, Japan, 2000), p. 131.
- [18] M. Mizoguchi, Charge and Orbital Ordering Structure of Fe₃O₄ in the Low-Temperature Phase as Deduced from NMR Study, *J. Phys. Soc. Jpn.* **70**, 2333 (2001).
- [19] V. Chlan, H. Štěpánková, R. Řezníček, and P. Novák, Anisotropy of hyperfine interactions as a tool for interpretation of NMR spectra in magnetic materials, *Solid State Nucl. Mag.* **40**, 27 (2011).
- [20] K. Abe, Y. Miyamoto, and S. Chikazumi, Magnetocrystalline anisotropy of low-temperature phase of magnetite, *J. Phys. Soc. Jpn.* **41**, 1894 (1976).
- [21] See Supplemental Material at <http://link.aps.org/supplemental/10.1103/PhysRevB.91.125134> for additional notes, figures, and tables.
- [22] S. Berger and S. Braun, *200 and More NMR Experiments* (Wiley-VCH, Weinheim, 2004).
- [23] M. Mizoguchi, NMR Study of the Low Temperature Phase of Fe₃O₄. I. Experiments, *J. Phys. Soc. Jpn.* **44**, 1501 (1978).
- [24] P. Blaha, K. Schwarz, G. K. H. Madsen, D. Kvasnicka, and J. Luitz, *WIEN2k, An Augmented Plane Wave + Local Orbitals Program for Calculating Crystal Properties* (Karlheinz Schwarz, Technische Universität Wien, Vienna, 2001).
- [25] P. Novák and V. Chlan, Contact hyperfine field at Fe nuclei from density functional calculations, *Phys. Rev. B* **81**, 174412 (2010).
- [26] S. Blügel, H. Akai, R. Zeller, and P. H. Dederichs, Hyperfine fields of 3d and 4d impurities in nickel, *Phys. Rev. B* **35**, 3271 (1987).
- [27] For clarity, Figs. 3, 5, and 7 in this work show the same trimerons as those plotted in Fig. 4 d in Ref. [10], and the coordinates of iron ions also follow those in Ref. [10]. On the other hand, Fig. 3 in Ref. [14] is offset (e.g., B1B2, which corresponds to B4 in our work, is not in the cell center), and a partly different set of trimerons is displayed, but it represents the same trimeron network. Unfortunately, there is no similar figure suitable for a straightforward comparison provided in Ref. [15].
- [28] R. F. W. Bader, *Atoms in Molecules: A Quantum Theory* (Oxford University Press, Oxford, 1990).